Aerosol Deposition of Ti₃SiC₂-MAX-Phase Coatings

Andreas Elsenberg[1] · Frank Gärtner[1] · Thomas Klassen[1]

Abstract For the present study on Aerosol Deposition of MAX-phase materials, Ti_3SiC_2 was chosen as model system due to the availability of property data and commercial powder. The as-received powder was milled to different nominal sizes. For revealing details on coating formation and possible bonding mechanisms, Aerosol Deposition experiments were performed for different particle size batches and process gas pressures. Microstructural analyses reveal that coating formation preferably occurs for particle sizes smaller two microns. Using such small particle sizes, crack-free, dense layers can be obtained. The individual deposition efficiencies for the different particle sizes, particularly the critical size below which deposition gets prominent, vary with process gas flows and associated pressures. Detailed microstructural analyses of coatings by high-resolution scanning electron microscopy reveal plastic deformation and fracture, both attributing to shape adaption to previous spray layers and probably bonding. In correlation to coating thickness or deposition efficiencies, respective results give indications for possible bonding mechanisms and a tentative window of Aerosol Deposition for Ti_3SiC_2 MAX-phases as spray material.

Keywords aerosol deposition · MAX-phase · process window · Ti_3SiC_2

✉ Andreas Elsenberg
Andreas.Elsenberg@hsu-hh.de

1 Helmut-Schmidt-University/University of the Federal Armed Forces, Holstenhofweg 85, 22043 Hamburg, Germany

Introduction

The rather new material class of MAX-phases combines properties of covalently bonded, brittle ceramics with those of metals. The metallic properties as machinability and electrical conductivity are due to atomic metal layers in the complex crystallographic structure. The general formula $M_{n+1}AX_n$ describes the composition with M as an early transition metal (Ti, Zr, Cr…), A as an A-group element (Si, Al…) and X as carbon or nitrogen. For potential applications, particularly Al-, or Cr-based MAX-phases are claimed to guarantee good oxidation protection up to temperatures of 1200 °C (Ref [1], [2]). Thus, MAX-phase materials can be considered for serving as protective coatings in a number of high-temperature applications (Ref [3-5]). However, so far, designed MAX phases are mainly deposited by thin film techniques, not reaching the needed thickness for ensuring long-term stability in harsh environments (Ref [6], [7]). In contrast to thin film techniques, powder spray methods are able to deposit layers in thickness of some tens to a few hundred of microns to fulfil the needs for corrosion or oxidation protection.

Common thermal spray processes operate with liquid phase deposition, and, thus, typically result in oxidation of the MAX-phase material and their decomposition into less protective compounds (Ref [8-13]). In contrast, kinetic spray methods like cold spraying (CS) or Aerosol Deposition (AD) can retain the original MAX-phase structure in the coating without oxidation (Ref [14-17]). For brittle, ceramic materials, particularly Aerosol Deposition has the potential for building up dense layers. As developed by Jun Akedo's group at the National Institute of Industrial Science and Technology (AIST) in Tsukuba, Japan in the 1990s (Ref [18], [19]), Aerosol Deposition is a kinetic spraying technology for small-sized ceramic materials operating with high-

velocity room temperature particle impact. Respective ceramic coatings can be applied to a variety of substrate materials, covering polymers, metals and ceramics (Ref 20). Up to now, a wide variety of ceramic materials was successfully buildup as layers using Aerosol Deposition (Ref 20).

Figure 1 shows a principle sketch of the Aerosol Deposition method. The fine powder is dispersed by an aerosol generator into the main process gas stream. As aerosol, this powder-gas mixture is then accelerated to high, eventually supersonic velocity by the flow through a, in most cases, converging nozzle with a straight exit regime, and the gas expansion into a vacuum chamber. In addition to providing high velocities, the expansion of the gas into vacuum should minimize bow shock effects in front of the substrate and powder from being carried away with the gas flow. However, as shown by sophisticated modelling by computational fluid dynamics (CFD), bow shock effects cannot be completely prevented in Aerosol Deposition (Ref 21-23). Thus, very small particles will suffer from deceleration and deflection in front of the substrate and, respectively, show lower impact velocities and deviations from optimum angle. More general information on the Aerosol Deposition method can be found in an overview article of Hanft et al. (Ref 20).

The bonding mechanisms for Aerosol Deposition are still controversially discussed. As used in cold spraying, ceramic particles are usually brittle and simply break at impact on the surface. However, Calvié et al. demonstrated that ceramic particles can plastically deform if their dimensions are in the nano-size regime (Ref 24). In practice, coating formation by Aerosol Deposition is associated with substantial grain refinement upon impact (Ref 18, 20); however, leaving some room for describing associated mechanisms. More recent work associates successful deposition with needed particle deformation (Ref 25-28).

So far, however, systematic investigations for MAX-phase coating formation by Aerosol Deposition are still missing. The only work on the topic reports successful deposition, but misses variation of process variables to provide a deeper understanding (Ref 29, 30). Thus, the major purpose of the present study is to provide information on the influence of primary particle size and applied process gas flow rates equivalent to process gas pressures on exceeding thresholds as critical velocities for successful coating formation. Detailed studies of coating microstructures, impact morphologies and surface topographies should help to distinguish associated bonding features, and to compare MAX-phase layer formation with so far established descriptions for coating formation of typical ceramic materials. Despite its lower oxidation resistance, Ti$_3$SiC$_2$ MAX-phase material was chosen as model system
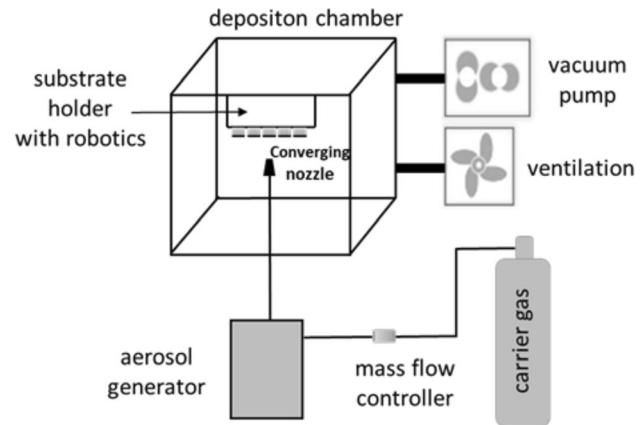

Fig. 1 Principle sketch of the Aerosol Deposition (AD) method

due to the availability of commercial powder and property data (Ref 31-33).

Materials and Experimental Procedures

Materials, Powder Milling and Particle Size Analysis

The Ti$_3$SiC$_2$ powder was produced by Sandvik/Kanthal, Sweden and pre-milled by Plansee, Germany, to sizes of D10 = 1.6 μm, D50 = 6.9 μm and D90 = 15.9 μm. For further size reduction, individual batches were milled with a planetary mill (Pulverisette 5/4 classic line) from Fritsch GmbH, Idar-Oberstein, Germany, by using zirconia grinding bowls and zirconia grinding balls in sizes of 2- and 10-mm. Milling was performed at 400 revs/min in isopropanol and frequently interrupted for cooling. The weight ratio of milling balls, powder and isopropanol as milling medium was set to 10:1:0.5 (with milling balls: 400 g; powder: 40 g; isopropanol: 20 g). For achieving different sizes, the milling times of the as-received powder were varied from 2 to 40 min.

The particle size distributions were measured by laser scattering using an instrument type LA-910 from Horiba, Kyoto, Japan. For these analyses, the powder was dispersed in distilled water.

Aerosol Deposition (AD)

Before spraying, the powders were dried in vacuum for 8 h at 250 °C and stored in a glove box to prevent the absorption of water. The Ti$_3$SiC$_2$ powder was sprayed by Aerosol Deposition in the as received and the differently milled conditions. Nitrogen was used as carrier and process gas at gas flows of 10, 15 and 20 l/min, corresponding to process gas pressures of 1.1, 1.4 and 1.8 bar, respectively.

The spraying distance was set to 15 mm and the substrates passed the Aerosol Deposition gas stream with a traverse speed of 5 mm/s. The base pressure of the vacuum chamber was kept at about 0.3 mbar. For assuring homogeneous surface coverage, a De Laval slit nozzle was used with nozzle throat dimensions of 4.0 mm × 0.2 mm. For powder feeding, a system of type RBG 1000ISD from Palas, Germany, was used. The powder feed rates were adjusted to about 3.8 cm^3/h.

Stainless steel AISI 304 plates with a thickness of 3 mm were used as substrates (lateral size 10 mm × 10 mm). The substrate surface was polished to a maximum surface roughness $R_a \leq 1$ μm. All substrates were cleaned in an ultrasonic bath with ethanol for 5 min. Remaining adsorbates on the surface were removed by plasma cleaning in oxygen atmosphere for 5 min. The substrates were coated with one, but also two and four layers to study possible erosion effects during multilayer deposition. For ensuring isolated particle impact events by a sort of wipe-test to study deformation morphologies, the powder feed rates and the traverse speed were drastically reduced to about 0.2 cm^3/h and 1 mm/s, respectively.

Estimation of Particle Velocities

For estimating particle velocities, the KSS software (Kinetic Spray Solutions, Germany, http://www.kinetic-spray-solutions.com/), originally designed for cold spraying, was here adapted for Aerosol Deposition. The software package is based on isentropic fluid mechanics to calculate gas and particle velocities, following procedures given in the literature (Ref 34-36), and on thermomechanical modeling to calculate critical velocities for bonding of metallic particles (Ref 37). For cold spaying, fine tuning of the fluid mechanical description was obtained by introducing correlation functions to match experimentally determined particle velocities, the details of computer codes being proprietary of KSS. It should be noted here that particle sizes and gas pressures applied in Aerosol Deposition reach the validity range of the models used in these calculations. Thus, respective results for Aerosol Deposition should be treated with care and just used as rough guideline for the influence of particle velocities. More sophisticated CFD-modelling using axisymmetric or two-dimensional approaches could reach better precision (Ref 21-23), but would need longer computational times.

Technically, the use of KSS software was adopted for Aerosol Deposition by considering the design of the specific nozzle as well as all boundary conditions of the experimental setup as input data. Properties of nitrogen as process gas were selected according to the KSS database. For calculating particle acceleration and heating and thus reachable velocities and temperatures, needed input data on the density of 4520 kg/m^3 and the specific heat of 562 J/(kg*K) of the Ti$_3$SiC$_2$ feedstock material were taken from the literature (Ref 31-33). The input data for individual powder sizes of the different batches were taken according to the results from laser scattering. For possible estimations of critical velocities and thermal softening of Ti$_3$SiC$_2$, the uniaxial compressive strength and the melting temperature were assumed to 1050 MPa (Ref 31-33) and 2650 °C, respectively, the later being calculated by GTT-Technologies, Herzogenrath, Germany. To avoid any uncertainty with respect to assumptions concerning the free flow and gas expansion into the vacuum chamber, the isentropic approach was selected to calculate particle velocities until the nozzle exit. As compared to the use of sonic nozzles with straight outlet and non-negligible acceleration in the free jet, such assumptions could be justified for using De-Laval spray nozzles. By applying De-Laval nozzles, most of the gas expansion and particle acceleration occurs already inside the expanding regime, and not in the free jet. Thus, additional effects by the flow distribution into the vacuum are less dominant. However, the here used continuum fluid dynamics can be only used as rough estimation, having limits for small particle dimensions and dilute fluid systems in vacuum by gas molecule free paths meeting particle sizes. In addition, such isentropic model cannot provide information on bow shock effects in front of the substrate. Thus, such calculations only provide an upper estimate for real impact conditions. As alternative approach, the KSS build-in algorithm for bow shock effects in cold spaying might be used for estimating impact velocities for particles reaching the substrate surface. Respective results, however, should be interpreted with care, since the software so far has not been calibrated for the small powder sizes and low pressures typically being in use for Aerosol Deposition.

Microscopy

Powder morphologies, coating microstructures and thickness were examined by high-resolution scanning electron microscopy (HR-SEM) using a dual-beam (electron-beam and ion-beam) Helios G4 UC from FEI, now Thermo Fisher Scientific Inc., Waltham, Massachusetts, USA. The acceleration voltage was adjusted to 10 kV. The different cross sections are prepared in situ in the HR-SEM by using the focused Ga$^+$-ion beam of the Helios G4 UC. For lower resolution, a SEM of type Quanta 650 from FEI, Netherlands was used at acceleration voltage of 20 kV.

The SEM cross-section micrographs were used for measuring the coating thickness by using the analyzing tools of the HR-SEM Helios G4 UC from FEI. Five measurements were performed to determine the mean coating thickness and the standard deviation.

Results

Powder Morphologies and Sizes

The micrographs in Fig. 2 show overviews and details of the morphologies of the different Ti_3SiC_2 powder size batches prepared for Aerosol Deposition. As produced by vibration milling, powder morphologies of the initial state are rather angular and fractured (Fig. 2a). Large particles more prominently have equiaxed shapes, whereas the smaller ones to higher extend are present as flat flakes. Independent of size, a significant amount of the particles shows lamellar-like pattern on the surface that could be interpreted as traces from deformation along distinguished planes, probably associated with dislocation gliding on the metallic lattice planes due to deformation during milling. Due to subsequent classification by air sifting, the initial batch does only contain minor amounts of fine sizes. By subsequent high-energy milling, smaller sizes are obtained as shown in Fig. 2(b), (c), (d), (e), (f) and (g). Already after short milling times and only slight mean size reduction, the batches contain rather significant amounts of fine particles with sizes < 1 μm (Fig. 2b, c). At the same milling time, using smaller ball sizes of 2 instead 10 mm results in more effective fracture of the larger particles and thus smaller mean sizes. In addition to size reduction, the particles more prominently show flat, platelet-like morphologies. With increased milling times, sizes get further reduced (Fig. 2d, e), the size distribution spreading from very fine particles to still some coarse ones. Particle surfaces appear fragmented; also a number of fine particles seem to adhere to the coarser ones. Interestingly, the individual shapes, particularly of the small ones, are more prominently equiaxed. As shown in Fig. 2(f) and (g), enhanced milling to smaller sizes mainly reduces the amount of larger particles. As before, attained shapes are angular with the majority being equiaxed. The formation of agglomerates might be supported by moisture left from isopropanol as milling additive.

Figure 3 shows the particle size distributions of the different milled powders used in this study to investigate the influence of particle size on the layer formation of Ti_3SiC_2 during Aerosol Deposition. The mean particle sizes cover a range from 6.9 μm (as received) to 0.5 μm (40 min milled with 2 mm zirconia balls). As already described for obtained powder morphologies, at same milling times, the use of smaller milling balls with diameters of 2 mm results in more effective size reduction than by using larger ones with sizes of 10 mm. For enhanced conditions, mainly the amount of larger particles is reduced, resulting in smaller mean sizes. Sizes of the D10 amount stay rather the same. This results in an overall more uniform size distribution for the batches of mean sizes of less than 2 μm, which could be important for avoiding possible surface damage by impact of larger particles in Aerosol Deposition.

Particle Velocities

Figure 4 summarizes the calculated particle velocities at nozzle exit (maximum particle velocity) for the different sizes and process conditions as obtained by an isentropic description using KSS software. The graph shows that particle velocities increase by about a factor of two within the range of decreasing mean sizes from about 15 to less than 3 μm. High velocities greater than 350 m/s are only obtained for particle sizes smaller than 2 μm. In contrast, the different process conditions seem to have only minor influence on particle velocity. The rise of process gas flow from 10 to 20 l/min and corresponding pressure results only in less than 40 m/s higher particle velocities. It should be noted here, that this comparison can only serve as rough guide, since effects by deceleration in the bow shock regime in front of the substrate are neglected in this simple approach. As compared to other publications, these calculated velocities could be treated as 'maximum velocities' as defined by Ma et al. (Ref 38). According to the so far assessable range by using KSS software for particle sizes down to 3 μm, bow shock effects reduce the impact velocities by maximum about 50 to 70 m/s, depending on gas flow rates, the bow shock effects being significantly smaller for larger ones. For smaller particle sizes down to of 1 μm or less, bow shock effects should reduce particle velocities by more than 100 m/s, as reported in the literature for Aerosol Deposition of Al_2O_3 by using N_2 as process gas under similar process conditions as in the present study (Ref 23).

Single-Layer Microstructures

Figure 5 summarizes SEM micrographs of the aerosol sprayed single-layer coatings as obtained under variation of the feedstock powder size and different spray conditions. As shown in the first three lines, no continuous coating is achieved for mean particle sizes in ranges from 6.9 to 4.4 μm. The situation cannot be improved by higher gas pressure. For continuous layers, mean particle sizes of less than 3.5 μm are needed, as shown in the fourth line, however, these coatings are very thin. The layer thickness being significantly smaller than mean particle size indicates that particles fracture at impact to smaller fragments. For the mean particle size of 3.5 μm, obtained layer thickness increases with gas pressure, ranging from 130 nm for 1.1 bar to 290 nm for 1.8 bar. Attainable coating thickness continues to increase with further decreasing mean particle

Fig. 2 SEM micrographs showing the morphologies of the Ti₃SiC₂ powders in as-received state (a), as well as for the different high-energy milling conditions for adjusting smaller sizes (b–g) for Aerosol Deposition
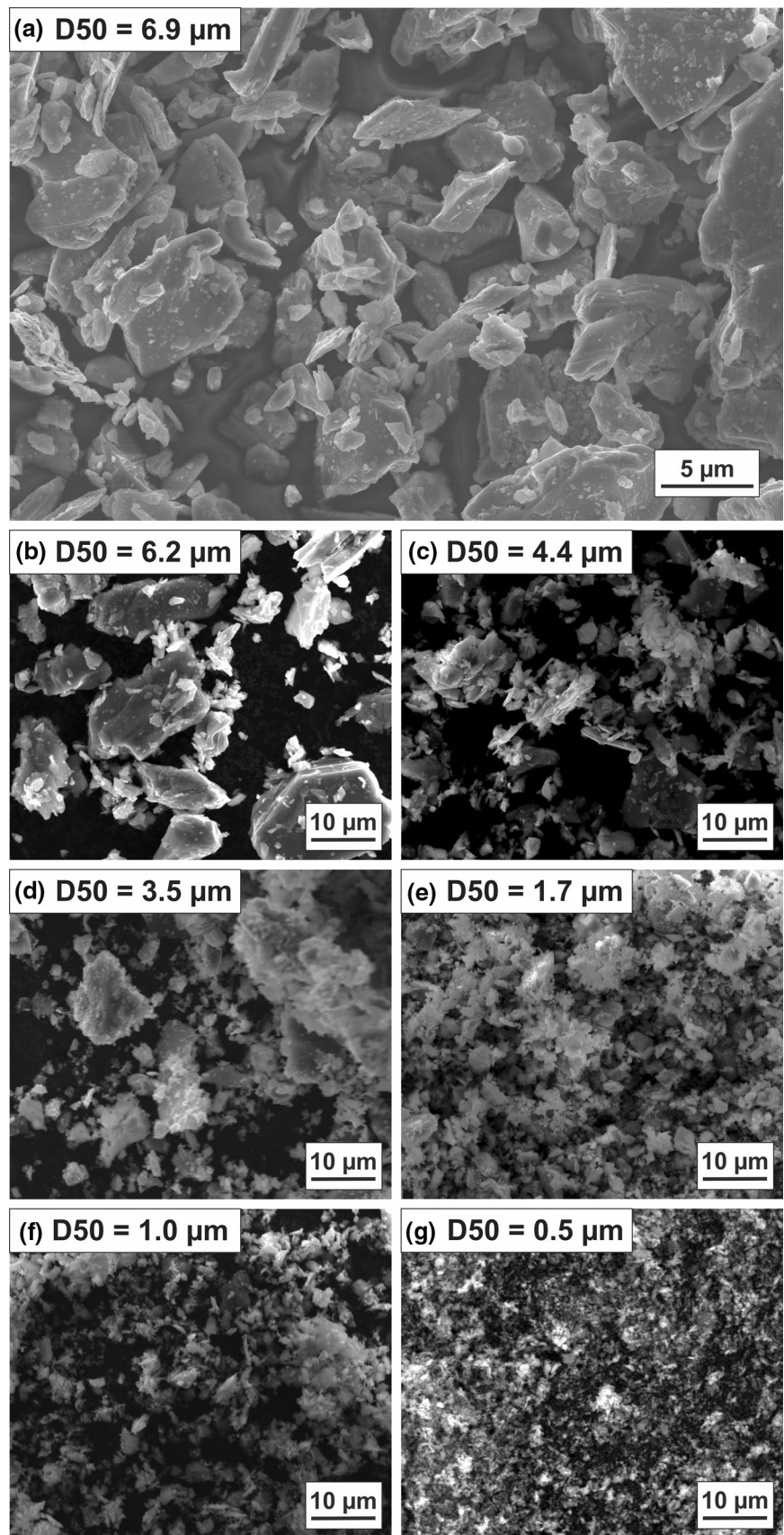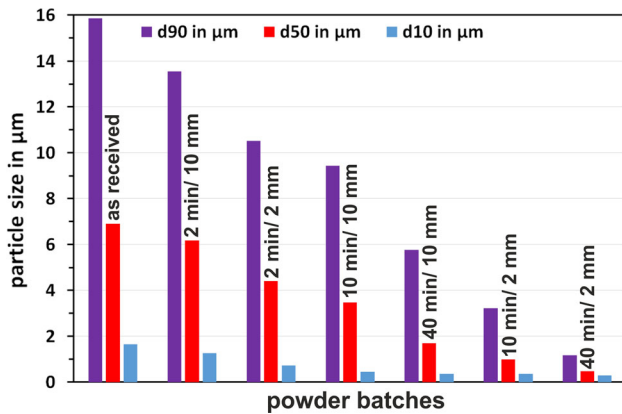
Fig. 3 Powder size distribution of Ti$_3$SiC$_2$ powders for aerosol spraying with D50 ranging from 6.9 μm (as received) to 0.5 μm (obtained by 40 min milling with 2 mm zirconia balls). Milling time and media sizes are indicated in the graph
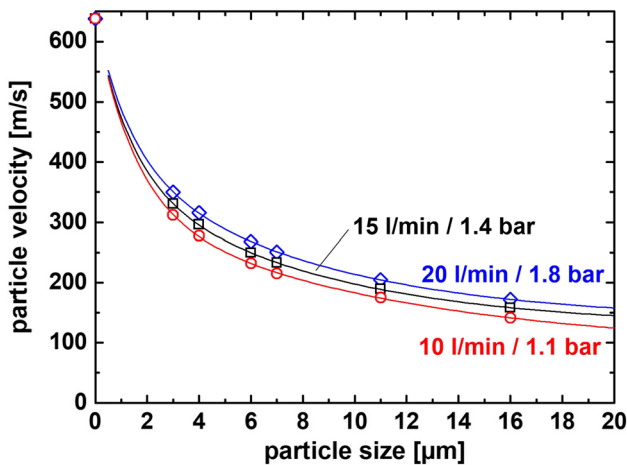

Fig. 4 Calculated maximum particle velocities as function of particle sizes for the different parameter sets used in Aerosol Deposition. The solid lines correspond to exponential fitting functions. The data points at zero size indicate the gas velocity and here serve as reference for curve fitting

sizes below 2 μm. It is interesting to note, that at similar sizes, deposition behaviors are comparable, independent from the powder process routes. The powders milled for forty minutes with 10 mm zirconia balls (Fig. 5, line 5) and a mean size of 1.7 μm results in a similar layer thickness as the powder with a mean size of 1.0 μm milled for 10 min with 2 mm zirconia balls (Fig. 5, line 6). They both achieve a coating thickness of 185 nm for a gas pressure of 1.1 bar, and a drastic coating thickness increase to 500-600 nm for higher gas pressures (1.4 and 1.8 bar). The major difference between the both concerns the amount of impurities, probably due to wear of milling media being more prominent for using larger balls. At a gas pressure of 1.1 bar, best layer buildup is observed for the finest powder (D50 = 0.5 μm) with a thickness of about 500 μm.

Unfortunately, due to problems with nozzle clogging occurring by using the finest powder (D50 = 0.5 μm), gas flows of 15 and 20 l/min (corresponding to process gas pressures of 1.4 and 1.8 bar) could not be continuously applied with this batch.
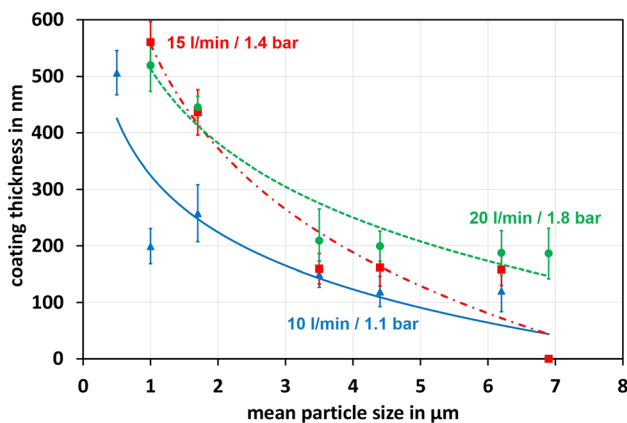
Figure 6 compares the single-layer thickness over the mean particle size for the three different flow rates or process gas pressures (10 l/min ≘ 1.1 bar in blue, 15 l/min ≘ 1.4 bar in red and 20 l/min ≘ 1.8 bar in green). The diagram clearly illustrates that the layer thickness increases for using smaller particle sizes. In addition, higher gas flow rates or gas pressures are beneficial for building up thicker layers. Particularly for small particles (< 2 μm), higher gas pressures of 1.4 and 1.8 bar lead to an about three times higher layer thickness as compared to that by using a gas pressure of 1.1 bar. More efficient layer buildup by using higher process gas pressures could be attributed to slightly higher particle velocities.

Multilayer Deposit Buildup

Figure 7 shows SEM images (25.000x) of single- (a), two- (b) and four-layer (c) coatings. As far as erosive effects of secondary particle impacts play no dominant role, coating thickness should increase for applying several passes or layers. The coatings shown here are processed by Aerosol Deposition at a gas flow rate of 10 l/min, corresponding to a p$_{gas}$ = 1.1 bar, using the Ti$_3$SiC$_2$ powder with a mean size of 1.7 μm. The comparison reveals that the coating thickness increases with the number of spray layers. The micrographs also disclose that a significant amount of impurities is present within the coatings, there being visible as white dots within the gray matrix. By EDS analyses, these impurities are identified as zirconia remnants from the milling balls.

For the example of using Ti$_3$SiC$_2$ powder with a mean size of 1.7 μm (40 min milled with 10 mm zirconia balls) in Aerosol Deposition, Figure 8 shows the coating thickness over the number of spray layers. The graph reveals linear correlations for the range of the single-, two- and four-pass coatings at all three process conditions (10 l/min ≘ 1.1 bar in blue, 15 l/min ≘ 1.4 bar in red and 20 l/min ≘ 1.8 bar in green). For the lowest process condition (10 l/min ≘ 1.1 bar), the coating thickness increases from 0.2 to 1.9 μm. The higher ones (15 l/min ≘ 1.4 bar, 20 l/min ≘ 1.8 bar) result in a greater two times more efficient deposition and an increase in coating thickness from 0.5 to 4.5 μm. The linear increase with the number of spray layers demonstrates that building-up thicker Ti$_3$SiC$_2$ coatings is possible, and within the investigated range not prominently affected by crack formation in already deposited layers and erosion under following impacts. The results for the higher process conditions barely differ,

D50 [μm]	Gas flow / process gas pressure		
	10 l/min / 1.1 bar	15 l/min / 1.4 bar	20 l/min / 1.8 bar
6.9			
6.2			
4.4			
3.5			
1.7			
1.0			
0.5			2 μm

Fig. 5 SEM micrographs of Ti_3SiC_2 layers processed by Aerosol Deposition using different particle size cuts (lines) and process gas pressures (columns). Continuous layer formation is only possible for particle sizes of < 2 μm, and best for medium process gas pressures. However, too fine powder sizes < 1 μm lead to problems in powder flow and nozzle clogging

Fig. 6 Layer thickness over the mean particles size for the three different flow rates or process gas pressures (10 l/min $\hat{=}$ 1.1 bar in blue, 15 l/min $\hat{=}$ 1.4 bar in red and 20 l/min $\hat{=}$ 1.8 bar in green). The diagram indicates that coating formation is only possible for small particle sizes (< 2 μm) and that the coating thickness increases with higher gas pressures

whereas an increase in the gas pressure from 1.1 to 1.4 bar improves the coating thickness by more than a factor of two. The improvement of the coating thickness for higher pressures can be attributed to the slightly higher particle velocity and thus higher kinetic energy upon impact, but might run into a saturation regime. On the basis of present data, it cannot be distinguished, whether such saturation of layer thickness at higher gas pressures is due to crack formation and erosion getting more prominent, or whether bow shock effects in front of the substrate more effectively attribute to particle deceleration.
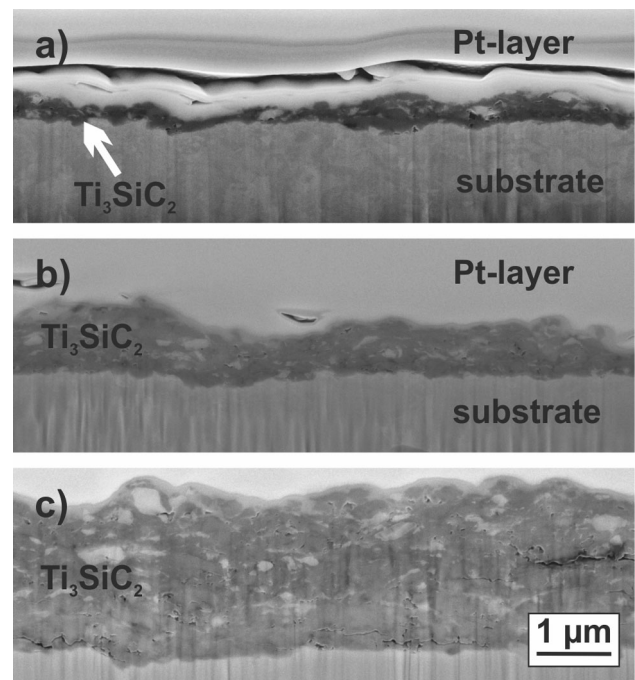

Fig. 7 SEM micrographs (25.000x) of single- (a), two- (b) and four-layer (c) coatings processed by Aerosol Deposition of Ti_3SiC_2 powder with a mean size of 1.7 μm (40 minutes milled with 10 mm zirconia balls) at a gas flow rate of 10 l/min, $p_{gas} = 1.1$ bar. The micrographs reveal an increase of thickness with number of layers. The bright spots within the gray matrix correspond to ZrO_2 impurities

Single Impact Morphologies

Figure 9 summarizes typical morphologies as obtained by primary impacts of Ti_3SiC_2 particles of different sizes onto the steel substrates. Since single impact morphologies of

the different particle sizes do not differ for the range of process conditions, individual distinction has been omitted. As shown in panel a and b, particles larger than 4 μm show similar features as the medium-sized ones, with fracture and internal deformation. Interestingly, some of the surface pattern show smoothened topographies that indicate viscous-like deformation phenomena, as so far observed in cold spraying of softer MAX-phase material as Ti_2AlC and Cr_2AlC (Ref 17). As shown in panel c, in the size range of 2-4 μm, most of the particles fracture into smaller pieces. However, fracture is always accompanied by deformation and surface laminae pattern. An example, focusing on the internal deformation, is given in panel d, and illustrates the deformation inside grains along characteristic shear planes and associated fracture phenomena. On the one hand, shear on the slip bands causes delamination. On the other hand, brittle, perpendicular cracks through the covalent bonded ceramic layers are observed. As given in panel e, very fine bonded particles with sizes smaller 0.1 μm have the same morphology as the feedstock powder, showing no traces of fracture or deformation. In sizes larger than about 0.5 μm, the impacted particles most prominently fracture and also show surface laminae pattern corresponding to the deformation along characteristic shear planes of the MAX phase structure, as indicated in panel f.

Deposit Surface Coverage and Morphologies

As shown by the layer microstructures in the cross sections, the success in deposit buildup shows drastic changes depending on particle sizes and to some extend by spray
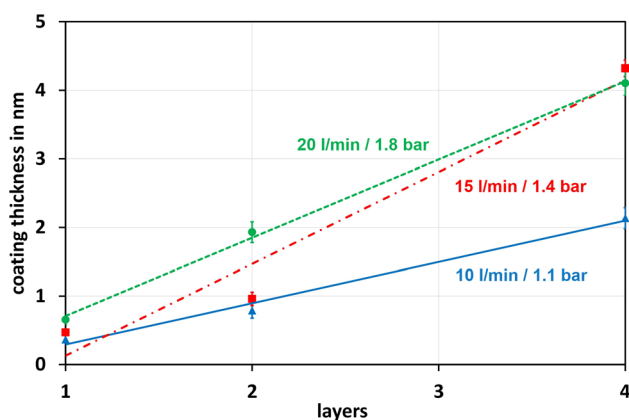

Fig. 8 Coating thickness over the number of spray layers by Aerosol Deposition of Ti_3SiC_2 powder with a mean size of 1.7 μm (40 min milled with 10 mm zirconia balls) as applied for the three different process conditions (10 l/min ≙ 1.1 bar in blue, 15 l/min ≙ 1.4 bar in red and 20 l/min ≙ 1.8 bar in green). The diagram reveals a linear increase in thickness with the number of spray layers for the single-, two- and four-layer coatings for all three gas pressures. In addition, it demonstrates that the coating thickness increases by using higher gas pressures

parameter sets. For supplying more global views on layer formation, Figure 10 shows SEM top view micrographs as obtained by the backscattering electron (BSE) mode to illustrate the surface coverage for the transition regime with respect to a particle size of 4.4 μm and spray conditions with gas flow rates of 10 to 20 l/min (a–e) for the deposition of one single layer. For supplying a suitable reference, respective analyses were performed at the edge to non-covered substrate surfaces showing the steel in bright contrast, the deposits in medium gray. As shown for a flow rate of 10 l/min in panel a and b, the substrate is heavily deformed under the impact of the MAX-phase particles. As illustrated by the medium gray contrast in panel b, only few sites can be revealed that correspond to bonded Ti_3SiC_2 powder or respective fragments. By increasing the flow rates to 15 l/min and 20 l/min, more of the MAX-phase material gets bonded, as visible by the increased amount of medium gray areas in panels c–f. Figure 11 shows an example for Aerosol Deposition of the Ti_3SiC_2 powder batch with a mean size of 1.0 μm, deposited as one layer at a gas flow rate of 15 l/min. Despite the rather rough surface topography given in panel a, the homogenously medium gray contrast of the BSE in panel b reveals complete surface coverage. For this particle size, the surface coverage is similar for using lower (10 l/min) or higher (20 l/min) gas flow rates (for the sake of space not shown here).

For building up thicker, well-bonded Ti_3SiC_2 layers by small particle sizes using Aerosol Deposition, however, internal stresses and weak adhesion to the substrate could result in local coating delamination of lateral extensions of up to 200 μm. A respective example for Aerosol Deposition with mean particle sizes of 1.0 μm deposited as one layer at a gas flow rate of 15 l/min is shown in Fig. 12. The BSE-contrast in panel b illustrates that within the regime of local layer spallation, failure mainly occurs at the interface to the substrate here revealing similar bright contrasts as for pure substrate material (compare Fig. 11). Locally slightly darker contrast within the spallation area can be attributed to some adhering, primary particles or deposited ones after spallation.

The primary single impacts onto the substrate shown in Fig. 9 could be influenced by the plastic deformation of the steel, and possibly associated less particle deceleration than obtained during impacts onto MAX-phase layers. For elucidating the particle deformation behavior during coating buildup, typical surface morphologies after deposition of one layer by using powders with mean sizes of 4.4, 1.0 and 0.5 μm at gas flow rates of 10 l/min (p_{gas}: 1.1 bar) are shown in the selection of high-resolution micrographs as top and under angular views in Fig. 13. As illustrated by panels a and b, multiple impacts of particles with a mean size of 4.4 μm mainly cause substrate deformation and

Fig. 9 Typical single impact morphologies under angular view of the SEM as obtained for Aerosol Deposition of different Ti_3SiC_2 powder particle sizes (a, b: large > 4 µm, c, d: medium 2-4 µm, e, f: small < 2 µm). Since single impact morphologies do not differ for the range of process conditions with gas flows of 10 l/min ≙ 1.1 bar, 15 l/min ≙ 1.4 bar and 20 l/min ≙ 1.8 bar. Thus, individual distinction has been omitted. The inserts describe: i: craters left in the substrate by non-successful impacts, ii: viscous-like flow pattern , iii: cracks, iv: deformation on laminae, v: fractured lamellas, vi: adhesion of complete, non-flattened particles, vii: fractured particles
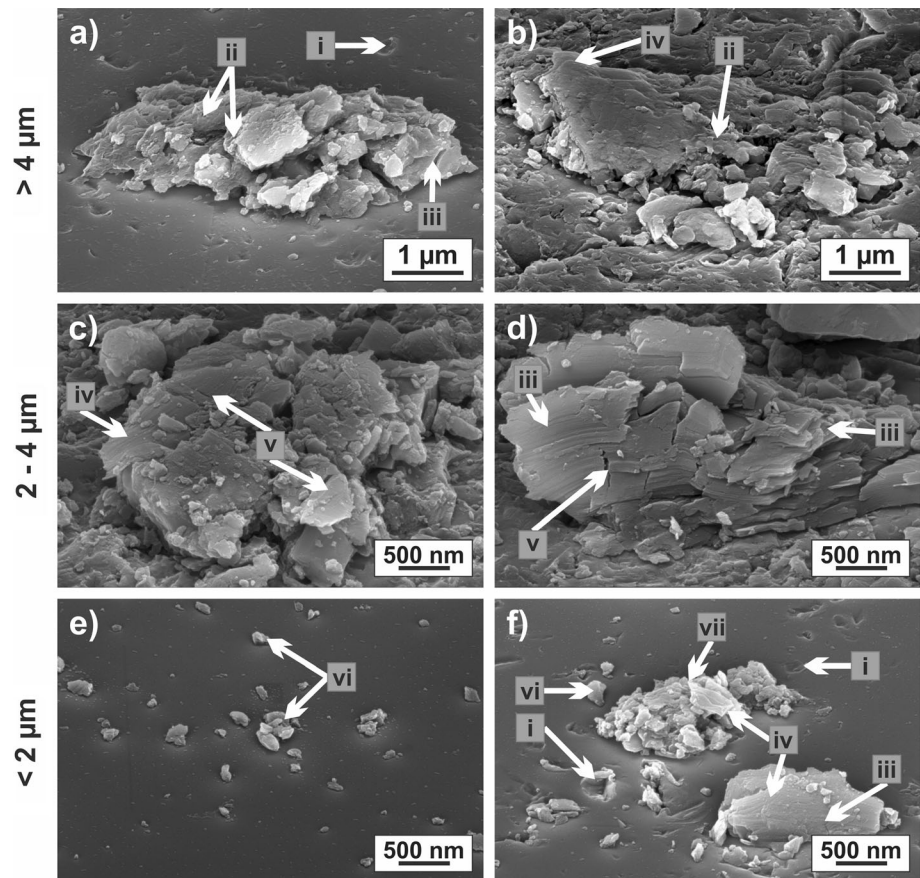
erosion. Particularly the top view reveals angular indents in the substrate surface left by non-successful particle impacts. Only few particles or particle remnants adhere to the surface. Judging from the angular view in panel b, sizes of these adhering remnants are smaller than those obtained under the single impact events of comparable sizes shown in Fig. 9(c) and (d). In addition, the Ti_3SiC_2 fragments under multiple impact show a smoother surface and less traces of cracks or fracture sites than those of primary adhering ones. Such could be attributed to fracture and deformation of adhering MAX-phase material under following high-velocity bombardment by particles of similar mechanical strength. Depositing the finer powder with a mean size of 1.0 µm, complete surface coverage is obtained (compare Fig. 11). Thus, surface morphologies do not show any traces of substrate deformation. According to the top view in panel c, most particle remnants on the surface appear flattened. The angular view in panel d allows for a better distinction between rather smooth areas in the valleys of surface topographies and hills building up by highly deformed particles. The sizes of the observed particle remnants are smaller than the respective initial particle sizes and than those of the single impact morphologies given in Figs. 2 and 9. In addition, only very few traces of particle deformation are observed. Some more loosely bonded particle on the hills might be due to rather recent impacts, not suffering from possible removement under follow-up impacts. Similar applies to the only few, mostly rather small pieces that roughly retain the original shape. The surface morphologies of the coating deposited by using the powder with a mean size of 0.5 µm show the same features as the one processed by using the slightly larger powder of 1.0 µm in size. Major differences concern local remnant surfaces having a smoother appearance and hills more prominently building up in extensions larger than original particle sizes.

Discussion

Prerequisites for Layer Formation

By systematic variation of mean powder sizes and spray conditions, key pre-requisites for Ti_3SiC_2 coating formation by Aerosol Deposition can be identified. From deposit cross section and surface coverage analyses, it can be judged that small mean particle sizes in a range of 0.5 to maximum 2 µm are essential for layer buildup. In addition, higher gas flow rates equivalent to higher process pressures occur as beneficial for coating formation. Based on the

Fig. 10 Single-layer surface topographies as obtained in top view by secondary electron mode (left) and the backscattering electron mode (right) of the SEM to illustrate the surface coverage as obtained for Aerosol Deposition of Ti_3SiC_2 powder of a mean size of 4.4 μm for parameter sets of (a, b) 10 l/min, (c, d) 15 l/min and (e, f) 20 l/min (a–e)
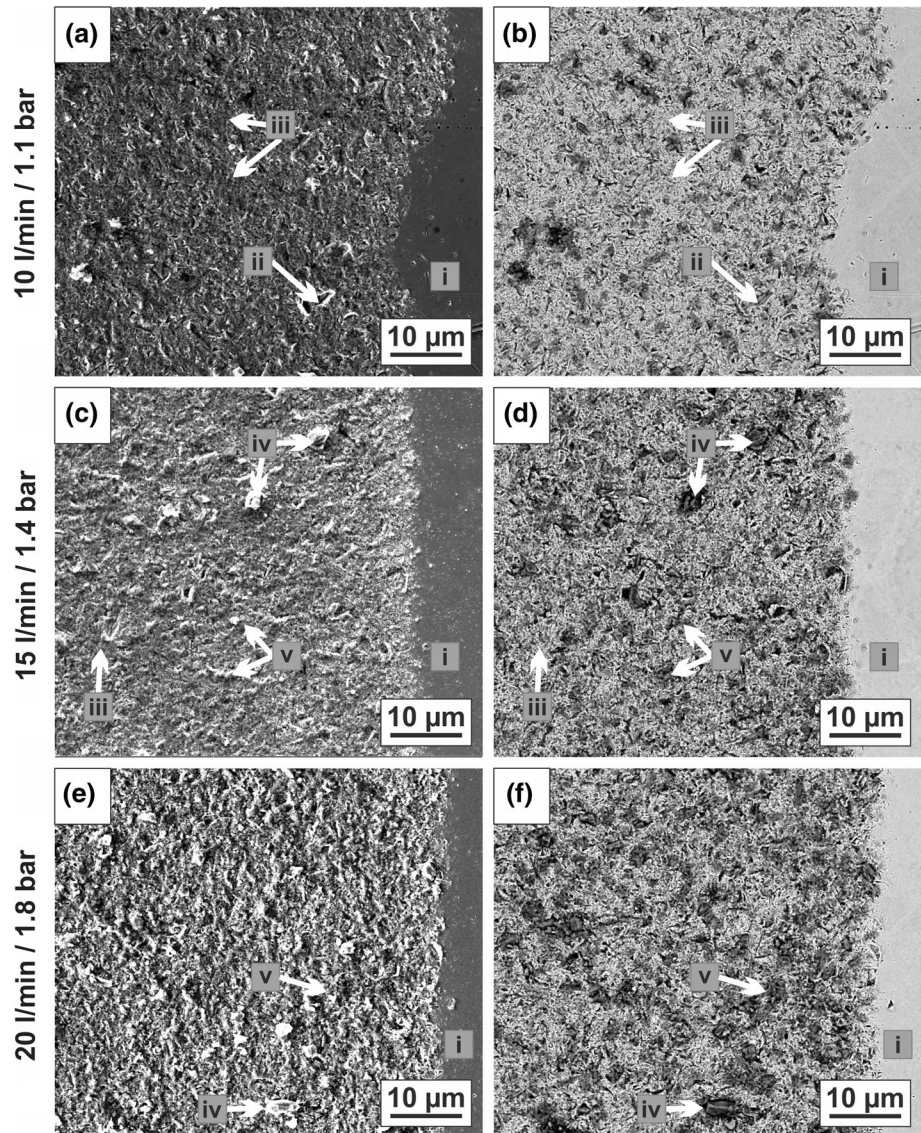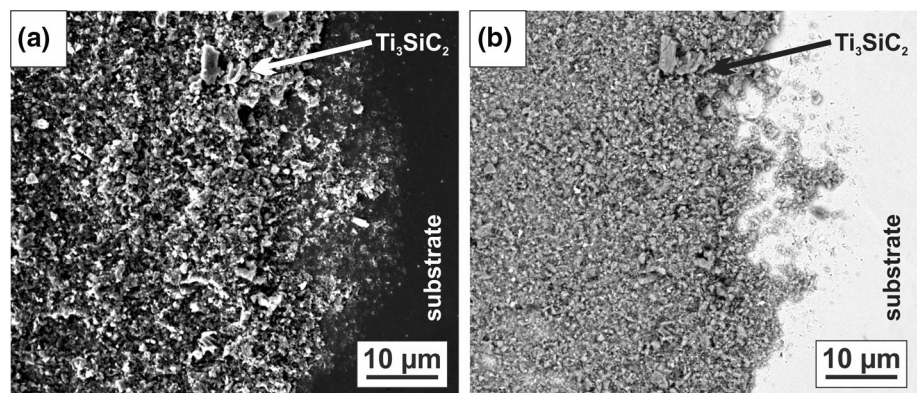

Fig. 11 Surface topographies as obtained in top view by secondary electron mode (a) and the backscattering electron mode (b) of the SEM illustrating the surface coverage as obtained for Aerosol Deposition of Ti_3SiC_2 powder with a mean size of 1.0 μm as deposited as single layer at gas flow rate of 15 l/min


development of coating thickness, the present data allow for developing a process window for successful Ti_3SiC_2 coating formation by Aerosol Deposition, despite all the statistical uncertainty and scatter of the data shown in Fig. 5 and 6.

Defining continuous layer formation and a single-layer thickness of 400 nm as threshold for coating formation,

Fig. 12 Surface topographies as obtained in top view by secondary electron mode (a) and the backscattering electron mode (b) of the SEM showing an area of local coating spallation and respective surface coverage as obtained for Aerosol Deposition of Ti_3SiC_2 powder in a mean size of 1.0 µm deposited as single layer at gas flow rate of 15 l/min
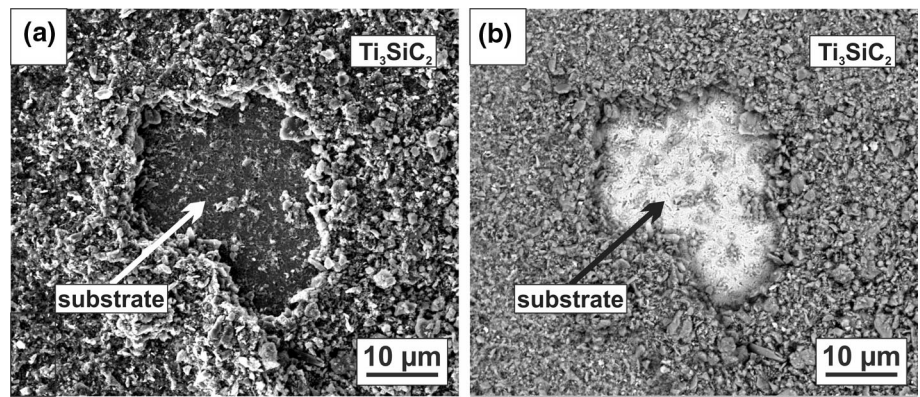
Fig. 13 High-resolution micrographs of surface topographies as obtained in top views (left) and angular view (right) after single-layer deposition of Ti_3SiC_2 powders in sizes of (a, b) 4.4 µm, (c, d) 1.0 µm and (d, e) 0.5 µm at Aerosol Deposition gas flow rates of 10 l/min. The different features on the surface are distinguished as i) craters in substrate surface, ii) recent Ti_3SiC_2 remnants, iii) valley of flat Ti_3SiC_2 layer after multiple follow-up impacts, iv) hill of adhering Ti_3SiC_2 particles by recent impacts, and v) very fine particles adhering to the surface showing minor deformation
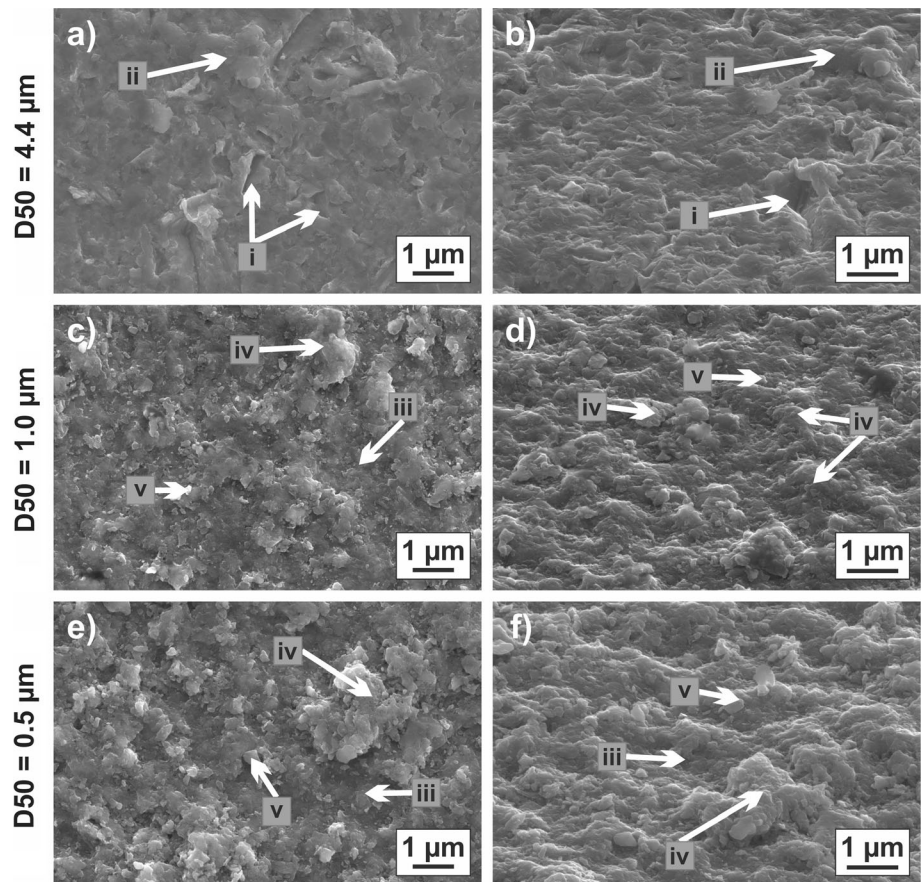

Fig. 14 illustrates respective regimes in terms of a process map. As stated above, successful deposition is only possible for small particles with D50 < 2 µm, using sufficiently high gas flow rates/process gas pressures ≥ 15 l/min/1.4 bar. The comparison for the different powder batches in the process map reveals that the regime for coating formation can be extended to lower parameter sets with a gas flow/process gas pressure of 10 l/min/1.1 bar, if mean particle sizes ≤ 1.0 µm are used in the Aerosol Deposition process. The derived range of successful Ti_3SiC_2 coating formation can be associated with a needed critical maximum particle velocity of about 350 m/s to achieve bonding (compare Fig. 4). The rise of gas flow/process gas pressure from 10 l/min/1.1 bar to 20 l/min/1.8 bar ensures slightly better particle acceleration, but only increases particle velocities differences by less than 40 m/s. However, the extended range of successful layer formation indicates that such increase could be decisive for reaching thresholds for bonding. Thus, the size regime for bonding could be slightly extended to larger particle diameters by using higher gas flow rates/gas pressures.

However, with respect to increased gas flow/process gas pressure, also possible upper borders by surface erosion or bow shock effects are expected, but respective experiments are still under investigation. Similar applies to the minimum particle size needed for deposition. However, with respect to very small sizes of less than 0.2 μm, the single impact morphologies and the surface topographies already indicate that such particles would adhere only loosely bonded and sparely deformed to the surface, in this condition probably not withstanding possible erosion by following impacts during coating formation. This is in agreement to reports in the literature for Aerosol Deposition by Hanft et al., associating successful deposition with fracture and grain refinement that should only occur for sizes ≳ 0.2 μm (Ref 20, 39). In comparison to the reported results for Aerosol Deposition of conventional ceramics, the present data for Ti_3SiC_2 show rather similar size ranges for successful layer formation. The described borders of powder sizes and process conditions for successful layer formation are in agreement to reports on Aerosol Deposition of ceramic materials (Ref 19, 20, 28). The estimated critical velocity of about 350 m/s for bonding of Ti_3SiC_2 is rather similar to values as reported by Kwon et al. for Aerosol Deposition of ceramic materials as Al_2O_3 and SiO_2 with 400 and 300 m/s, respectively (Ref 28). Bonding of Ti_3SiC_2 meeting the same range of critical velocities underlines a predominantly ceramic behavior of this type of MAX-phase material. With respect to influences by particle deceleration due to bow shock effects (Ref 21-23), it should be noted here that real impact velocities, depending on particle sizes, should be by about 50 to 100 m/s lower than given here in the rough estimates.

The in comparison to literature more ceramic-like behavior of Ti_3SiC_2 indicates that the specific crystal structure with weaker metal layers, at least for this type of MAX-phase, is not playing a dominant role for bonding
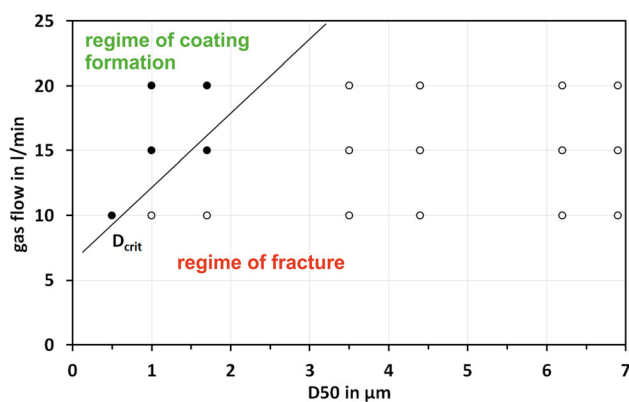
and layer formation by Aerosol Deposition. However, the situation could be different for other MAX-phase materials that allow for more distinct plastic deformation along less strongly bonded metallic crystal planes. Recent investigations by cold spraying revealed significant differences in particle deformation and possible layer formation depending on MAX-phase type and associated compressive strengths (Ref 17) and indicated a more ceramic-like behavior for Ti_3SiC_2.

For Aerosol Deposition of ceramics in general, several models are discussed to explain bonding. By experiments and modelling, most established descriptions associate bonding and layer formation in Aerosol Deposition with (dynamic) particle fragmentation into nanocrystalline microstructures (Ref 19, 20, 28). Another approach was followed by Daneshian et al. by using molecular dynamic (MD) simulations (Ref 40, 41). For nanoparticle impact, their computations distinguish regimes of (i) rebound (ii) deformation and bonding and (iii) particle fracture, whereas only deformation associated effects are defined to contribute to layer formation. Here, the critical velocity is defined as the transition between (i) rebound and (ii) deformation and bonding. In addition, they argue on fragmentation at very high velocities, and trends for this being more prominent for larger particle sizes.

Up to now, exploring Aerosol Deposition of Ti_3SiC_2 with mean particle sizes < 1 μm is still challenging. Particle sizes < 1 μm lead to process instabilities by discontinuous powder flow, and thus in nozzle clogging and pressure fluctuations. In present investigations, this was more prominent for using higher process conditions with gas flows/process gas pressures ≥ 15 l/min ≘ 1.4 bar, here not allowing for continuous flow. Also, at the lower gas flow/process gas pressure of 10 l/min/1.1 bar, flow and pressure fluctuations occur. Varying particle velocities during the process result in coating defects as pores, cracks and non-bonded zones, as shown in Fig. 15. Current investigations concern possible counter-measures to improve process stability by tuning powder flowability and optimizing gas flow for avoiding clogging in tubes or nozzles.

Microscopic Deformation Features

The results of the present study demonstrate that continuous and rather dense Ti_3SiC_2 layers can have a thickness significantly smaller than the mean particle size (thickness ≪ 500 nm, particle size > 1 μm). This indicates that coating formation to rather high extent is associated with particle fracture and grain refinement, in agreement with reports from the literature (Ref 18, 20). This is no contradiction to assuming a critical threshold velocity for bonding, with a maximum particle size of about 2 μm. Size

Fig. 14 Process map for Aerosol Deposition of Ti_3SiC_2. The solid dots indicate successful coating formation by exceeding a single-layer thickness of 400 nm resulting in continuous single-layer formation. Hollow dots indicate non-continuous layers

effects determine maximum velocities at given process parameters. In turn, impact velocities can govern fracture or plastic deformation at high strain rate for ceramics. Furthermore, too large particles might simply break due to their brittle ceramic behavior, just causing deformation or leaving remnants on the substrate surface (compare Figure 5, upper 3 lines), while small ones with sizes $\lesssim 2$ µm might be able to show at least partial plastic behavior.

The analyses of single impact morphologies confirm that most adhering Ti_3SiC_2 particles fracture into smaller pieces. Only very small ones with sizes of about less than 0.2 µm seem to retain their size (see Fig. 9). The fracture to high extent is associated to brittle failure across the covalent bonded ceramic layers of the crystal structure. Plastic-like deformation on the metallic lattice layers seems to attribute to flattening and in some instance to internal delamination. Only in very few cases, viscous-like flow phenomena as achievable under thermal softening by high strain rate plastic deformation are observed. Thus, the layer formation of Ti_3SiC_2 particles in Aerosol Deposition is mainly associated with ceramic-like fracture. However, with about 100 to 500 nm, the size of fragments obtained in single impacts is much larger than refinement sizes of less than 20 nm reported in the literature for successful layer formation by Aerosol Deposition (Ref 19, 28, 42). Thus, the single impact morphologies showing the whole particle are probably not representative for the mechanisms associated with dense layer formation. One hint on that can be gained by the amounts of adhering material. Under single
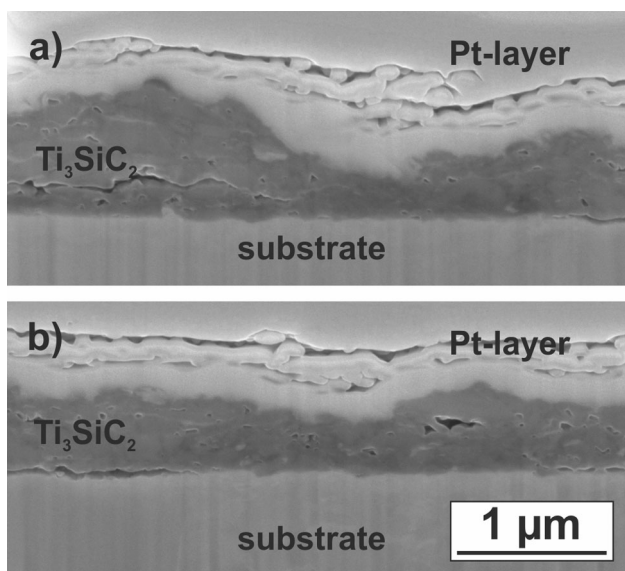

Fig. 15 SEM micrographs (50.000x) of different locations within the Ti_3SiC_2 layer processed by Aerosol Deposition using the finest powder (D50 = 0.5 µm) at a gas flow/process gas pressure of 10 l/min $\triangleq$ 1.1 bar. The layer shows pores, cracks and non-bonded zones in the coating due to the powder flow fluctuation during the spraying process

impacts of particles smaller 2 µm, more than half of the events results in successful adhesion to the substrate, corresponding to a deposition efficiency (DE) greater than 50%. In contrast, deposition efficiencies obtained to complete layer formation by Aerosol Deposition usually is typically lower than 1% (Ref 43, 44). This means that probably far more than 90% of the primarily adhering material is removed by erosion under the bombardment of secondary impacts. Thus, more insights into the stability of well-bonded material could be provided by top views onto adhering layers. For successful Ti_3SiC_2 layer formation using particle sizes ≤ 2 µm in Aerosol Deposition (see Fig. 13), the surfaces show rather flattened particles or particle remnants. Typical surface features are much smaller than original particle sizes. In addition, most of the features have a rather smooth appearance. This could be attributed to significant influence by secondary impacts that remove loosely bonded parts of adhering particles and might attribute to more deformation and refinement of already well-bonded material. Only few parts on the surface appear more loosely bonded. These might be associated with rather recent impact events that so far not got subjected to complete or partial erosion. The slightly rougher surface topography for depositing finer powder sizes might be attributed to local differences in bow shock phenomena preferably decelerating smaller particles in front of local valley regimes. In summary, the observations for Aerosol Deposition of Ti_3SiC_2 correspond well to the impact models by Akedo, Hanft et al. or Kwon et al. (Ref 19, 20, 28), postulating heavy deformation and refinement being more prominent close the interface between adhering material and the impacting particle, and immediate or later removement of upper parts by fracture or erosion.

General Remarks

Most of above reflections deal with rather ideal cases. It should be noted here, that all powder batches represent a distribution of particle sizes. Therefore, multiple effects might be present in one layer. In consequence, wide particle size distributions should be avoided. Too large particles could cause layer erosion and contribute to local crack formation. In addition, surface topographies could enhance bow shock effects, means bigger particles reaching and eroding less well-bonded surfaces in local valleys, which are buildup by decelerated and less than optimum bonded small ones. In addition, the local stress management and deposit adhesion are a matter for improving process stability. Partial layer spallation indicates the presence of compressive stresses and a lack of local adhesion. Both might be tuned by surface modification and additional thermal management during deposition.

In addition, the present results demonstrate that powder production and refinement can cause contaminations by the milling media (compare Fig. 7). Thus, further work is needed to optimize powder production to allow for a better distinction of effects leading to layer formation. Nevertheless, the present study demonstrates the possibility to develop a process selection map for Aerosol Deposition of Ti_3SiC_2. Using most promising spray parameter sets, the application of several layers can be used to reach a coating thickness of several microns to fulfill the demands in possible applications. Parts of the gained knowledge concerning basic principles should be also valid for other MAX-phase materials.

Summary and Conclusions

The present study presents a comprehensive investigation on Aerosol Deposition to process Ti_3SiC_2 MAX-phase coatings. By applying a range of spray conditions to a variety of powder sizes, prerequisites for successful layer deposition are worked out and presented in the form of a process map. The results show that coating formation is only possible for particle sizes below 2 μm. Individual deposition rates depend on process conditions, such as gas flow rates corresponding to process gas pressures, the field of successful coating formation being larger for higher pressures. Successful bonding can associated with particle impacts exceeding a critical maximum velocity of about 350 m/s. By applying several spray layers, desired coating thickness for applications can be adjusted, here also proving process stability. According to all these results, the Ti_3SiC_2 MAX-phase behaves similar to typical ceramic material, with no detectable particular influence of the metallic crystal layers. Thus, it must be investigated in detail to which extend respective procedures for coating optimization should be transferable to Aerosol Deposition of other MAX-phase materials of lower compressive strengths.

References

1. D.J. Tallman, B. Anasori and M.W. barsoum, A Critical Review of the Oxidation of Ti2AlC, Ti3AlC2 and Cr2AlC in Air, *Mater. Res. Lett.*, 2013, **3**, p 115-125.
2. Z.M. Sun, Progress in Research and Development on MAX Phases: A Family of Layered Ternary Compounds, *Int. Mater. Rev.*, 2011, **56**(3), p 143-166.
3. M.W. barsoum and T. El-Raghy, The MAX-Phases: Unique New Carbide and Nitride Materials, *Am. Sci.*, 2001, **89**, p 334-343.
4. M. Radovic and M.W. barsoum, MAX Phases: Bridging the Gap Between Metals and Ceramics, *Am. Ceram. Soc. Bull.*, 2013, **61**(19), p 20-27.
5. M. Sundberg, G. Malmqvist, A. Magnusson, and T. El-Raghy, Alumina Forming High Temperature Silicides and Carbides, *Ceram. Int.*, 2004, **30**, p 1899-1904.
6. C. Walter, C. Martinez, T. El-Raghy, and J.M. Schneider, Towards Large Area MAX Phase Coatings on Steel, *Steel Res. Int.*, 2005, **76**(2), p 225-228.
7. P. Eklund, M. Beckers, U. Jansson, H. Högberg, and L. Hultman, The $M_{n+1}AX_n$ Phases: Materials Science and Thin-Film Processing, *Thin Solid Films*, 2010, **518**, p 1851-1878.
8. J. Frodelius, M. Sonestedt, S. Björklund, J.-P. Palmquist, K. Stiller, H. Högberg, and L. Hultman, Ti_2AlC Coatings Deposited by High Velocity Oxy-Fuel Spraying, *Surf. Coat. Technol.*, 2008, **202**(24), p 5976-5981.
9. J. Jiang, A. Fasth, P. Nylén, and W.B. Choi, Microindentation and Inverse Analysis to Characterize Elastic-Plastic Properties for Thermal Sprayed Ti_2AlC and NiCoCrAlY, *J. Therm. Spray Technol.*, 2009, **18**(2), p 194-200.
10. M. Sonestedt, J. Frodelius, J.P. Palmquist, H. Högberg, L. Hultman, and K. Stiller, Microstructure of High Velocity Oxy-Fuel Sprayed Ti_2AlC Coatings, *J. Mater. Sci.*, 2010, **45**, p 2760-2769.
11. R. Trache, R. Puschmann, C. Leyens, L.-M. Berger, B. Matthey, M. Herrmann, Thermally Sprayed Ti_3SiC_2 and Ti_2AlC MAX-Phase Coatings, *Thermal Spray 2013: Proceedings of the International Thermal Spray Conference*, R.S. Lima, A. Agarwal, M.M. Hyland, Y.-C. Lau, G. Mauer, A. McDonald, F.-L. Toma, Ed., May 13-15, 2013 (Busan, South Korea), ASM International, 2014, p 74-78

12. N. Markocsan, D. Manitsas, J. Jiang, and S. Björklund, MAX-phase Coatings Produced by Thermal Spraying, *J. Superhard Mater.*, 2017, **39**(5), p 355-364.

13. Z. Zhang, S.H. Lim, J. Chai, D.M.Y. Lai, P.C. Lim, A.K.H. Cheong, S. Wang, and HJin, J Pan, , Kerosene-Fuelled High Velocity Oxy-Fuel (HVOF) Spray of Ti2AlC MAX Phase Powders, *J. Alloys Compd.*, 2018, **735**, p 377-385.

14. H. Gutzmann, F. Gärtner, D. Höche, C. Blawert, and T. Klassen, Cold Spraying of Ti2AlC MAX-Phase Coatings, *J. Therm. Spray Technol.*, 2013, **22**, p 406-412.

15. B.R. Maier, B.L. Garcia-Diaz, B. Hauch, L.C. Olson, R.L. Sindelar, and K. Sridharan, Cold Spray Deposition of Ti2AlC Coatings for Improved Nuclear Fuel Cladding, *J. Nucl. Phys. Mater. Sci. Radiat. Appl.*, 2015, **466**, p 1-6.

16. T. Go, Y.J. Sohn, G. Mauer, R. Vaßen, and J. Gonzalez-Julian, Cold Spray Deposition of Cr2AlC MAX Phase for Coatings and Bond-Coat Layers, *J. Eur. Ceram. Soc.*, 2019, **39**, p 860-867.

17. A. Elsenberg, M. Busato, F. Gärtner, A. List, A. Bruera, G. Bolelli, L. Lusvarghi, and T. Klassen, Influence of MAX-Phase Deformability on Coating Formation by Cold Spraying, *J. Therm. Spray Technol.*, Special Issue on Aerosol Deposition and Kinetic Spray Processes, 2020, https://doi.org/10.1007/s11666-020-01110-w

18. J. Akedo, Ceramic Thick Films at Room Temperature: Densification Mechanism of Ceramic Layers, *J. Am. Ceram. Soc.*, 2006, **89**, p 1834-1839.

19. J. Akedo, Room Temperature Impact Consolidation (RTIC) of Fine Ceramic Powder by Aerosol Deposition Method and Applications to Microdevices, *J. Therm. Spray Technol.*, 2008, **17**, p 181-198.

20. D. Hanft, J. Exner, M. Schubert, T. Stöcker, P. Fuierer, and R. Moos, An overview of the Aerosol Deposition Method: Process Fundamentals and New Trends in Materials Applications, *Journal of Ceramic Science and Technology*, 2015, **06**, p 147-181.

21. S. Johnson, D. Schwer, D. Park, Y. Park, and E. Gorzkowski, Deposition Efficiency of barium Hexaferrite by Aerosol Deposition, *Surf. Coat. Technol.*, 2017, **332**, p 542-549.

22. H. Park, H. Kwon, and C. Lee, Inflight Particle Behavior in the Vacuum Kinetic Spray Process, *J. Therm. Spray Technol.*, 2017, **26**, p 1616-1631.

23. H. Park, H. Kwon, Y. Kim, and C. Lee, Computational Research on Factors Affecting Particle Velocity in a Vacuum Kinetic Spray Process, *J. Therm. Spray Technol.*, 2019, **28**, p 1945-1958.

24. E. Calvié, J. Réthoré, L. Joly-Pottuz, S. Meille, J. Chevalier, V. Garnier, Y. Jorand, C. Esnouf, T. Epicier, J. Quirk, and K. Masenelli-Varlot, Mechanical Behavior Law of Ceramic Nanoparticles from Transmission Electron Microscopy In Situ Nano-compression Tests, *Mater. Lett.*, 2014, **119**, p 107-110.

25. H. Park, J. Kwon, I. Lee, and C. Lee, Shock-Induced Plasticity and Fragmentation Phenomena During Alumina Deposition in the Vacuum Kinetic Spraying Process, *Scripta Mater.*, 2015, **100**, p 44-47.

26. H. Park, J. Kim, and C. Lee, Dynamic Fragmentation Process and Fragment Microstructure Evolution of Alumina Particles in a Vacuum Kinetic Spraying System, *Scripta Mater.*, 2015, **108**, p 72-75.

27. H. Park, J. Kim, S.B. Lee, and C. Lee, Correlation of Fracture Mode Transition of Ceramic Particle with Critical Velocity for Successful Deposition in Vacuum Kinetic Spraying Process, *J. Therm. Spray Technol.*, 2017, **26**, p 327-339.

28. H. Kwon, Y. Kim, H. Park and C. Lee, Impact Behavior for Successful Particle-Particle Bonding in Vacuum Kinetic Spraying, *J. Therm. Spray Technol.*, 2020 https://doi.org/10.1007/s11666-020-01078-7

29. M.A. Piechowiak, J. Henon, O. Durand-Panteix, G. Etchegoyen, V. Coudert, P. Marchet, and F. Rossignol, Growth of Dense Ti3SiC2 MAX Phase Films Elaborated at Room Temperature by Aerosol Deposition Method, *J. Eur. Soc.*, 2014, **34**, p 1063-1072.

30. J. Henon, M.A. Piechowiak, O. Durand-Panteix, G. Etchegoyen, C. Dublanche-Tixier, P. Dublanche-Ticier, M.B. Lucas, and F. Rossignol, Dense and Highly Textured Coatings Obtained by Aerosol Deposition Method from Ti3SiC2 Powder: Comparison to a Dense Material Sintered by Spark Plasma Sintering, *J. Eur. Soc.*, 2015, **35**, p 1179-1189.

31. M.W. barsoum, T. El-Raghy, C.J. Rawn, W.D. Porter, H. Wang, E.A. Payzant, and C.R. Hubbard, Thermal Properties of Ti3SiC2, *J. Phys. Chem. Solids*, 1999, **60**, p 429-439.

32. M.W. barsoum and M. Radovic, Elastic and Mechanical Properties of the MAX Phases, *Annu. Rev. Mater. Res.*, 2011, **41**, p 195-227.

33. M. W. barsoum, *MAX Phases—Properties of Machinable Ternary Carbides and Nitrides*, Ed. 1, Wiley-VCH, 2013

34. T. Stoltenhoff, H. Kreye, and H.J. Richter, An Analysis of the Cold Spray Process and its Coatings, *J. Therm. Spray Technol.*, 2002, **11**, p 542-550.

35. T. Schmidt, H. Assadi, F. Gärtner, H. Richter, T. Stoltenhoff, H. Kreye, and T. Klassen, From Particle Acceleration to Impact and Bonding in Cold Spraying, *J. Therm. Spray Technol.*, 2009, **18**, p 794.

36. H. Assadi, T. Schmidt, H. Richter, J.-O. Kliemann, K. Binder, F. Gärtner, T. Klassen, and H. Kreye, On Parameter Selection in Cold Spraying, *J. Therm. Spray Technol.*, 2011, **20**, p 1161-1176.

37. T. Schmidt, F. Gärtner, H. Assadi, and H. Kreye, Development of a Generalized Parameter Window for Cold Spray Deposition, *Acta Mater.*, 2006, **54**(3), p 729-742.

38. K. Ma, C.-J. Li and C.-X. Li, Narrow and Thin Copper Linear Pattern Deposited by Vacuum Cold Spraying and Deposition Behavior Simulation, *J. Therm. Spray Technol.*, 2020 https://doi.org/10.1007/s11666-020-01102-w

39. J. Exner, Aerosolbasierte Kaltabscheidung von Funktionskeramiken für neuartige Anwendungen im Bereich der Sensorik und Energiewandlung, 2019, **8**, *Prof. Dr.-Ing. Ralf Moos und Prof. Dr.-Ing. Gerhard Fischerauer, Bayreuth: Shaker Verlag GmbH*, german

40. B. Daneshian and H. Assadi, Impact Behavior of Intrinsically Brittle Nanoparticles: A Molecular Dynamics Perspective, *J. Therm. Spray Technol.*, 2014, **23**, p 541-550.

41. B. Daneshian, F. Gärtner, H. Assadi, D. Höche, W. Weber, and T. Klassen, Size Effects of Brittle Particles in Aerosol Deposition—Molecular Dynamics Simulation, *J. Therm. Spray Technol.*, 2021 https://doi.org/10.1007/s11666-020-01149-9

42. T. Hoshina, T. Furuta, Y. Kigoshi, S. Hatta, N. Horiuchi, H. Takeda and T. Tsurumi, Size Effect of Nanograined BaTiO3 Ceramics Fabricated by Aerosol Deposition Method, *Jpn. J. Appl. Phys.*, 2010, **49**, p 09MC02. https://doi.org/10.1143/JJAP.49.09MC02

43. K. Naoe, M. Nishiki, and A. Yumoto, Relationship Between Impact Velocity of Al2O3 Particles and Deposition Efficiency in Aerosol Deposition Method, *J. Therm. Spray Technol.*, 2013, **22**, p 1267-1274.

44. K. Naoe, K. Sato, and M. Nishiki, Effect of Process for Producing Al2O3 Particles on Deposition Efficiency in Aerosol Deposition Method, *J. Ceram. Soc. Japan*, 2014, **122**(1), p 110-116.